The Astrophysical Journal, 990:194 (14pp), 2025 September 10 https://doi.org/10.3847/1538-4357/adf5c1

X-Ray Halos of Early-type Galaxies with Active Galactic Nucleus Feedback and Accretion from a Circumgalactic Medium: Models and Observations

Silvia Pellegrini[1,2], Luca Ciotti[1], Zhaoming Gan[3], Dong-Woo Kim[4], and Jeremiah P. Ostriker[5,6,7]
[1] Department of Physics and Astronomy, University of Bologna, via Gobetti 93/2, I-40129 Bologna, Italy; silvia.pellegrini@unibo.it
[2] INAF-Osservatorio di Astrofisica e Scienza dello Spazio di Bologna, Via Gobetti 93/3, I-40129 Bologna, Italy
[3] New Mexico Consortium, Los Alamos, NM 87544, USA
[4] Harvard-Smithsonian Center for Astrophysics, 60 Garden Street, Cambridge, MA 02138, USA
[5] Department of Astronomy, Columbia University, 550 West 120th Street, New York, NY 10027, USA
[6] Department of Astrophysical Sciences, Princeton University, Princeton, NJ 08544, USA
Received 2025 May 29; revised 2025 July 21; accepted 2025 July 28; published 2025 September 9

Abstract

Knowledge of the X-ray properties of the hot-gas halos of early-type galaxies (ETGs) has significantly advanced in the past years, for large and homogeneously investigated samples. We compare these results with the X-ray properties of an exploratory set of gas evolution models in realistic ETGs, produced with our high-resolution 2D hydrodynamical code MACER that includes active galactic nucleus feedback and accretion from a circumgalactic medium. The model X-ray emission and absorption are integrated along the line of sight, to obtain maps of the surface brightness Σ_X and temperature T_X. The X-ray diagnostics considered are the luminosity and average temperature for the whole galaxy (L_X and $\langle T_X\rangle$) and within five optical effective radii ($L_{X,5}$ and $\langle T_{X,5}\rangle$) and the circularized profiles $\Sigma_X(R)$ and $T_X(R)$. The values for L_X, $L_{X,5}$, $\langle T_X\rangle$, and $\langle T_{X,5}\rangle$ compare very well with those observed. The $\Sigma_X(R)$ and $T_X(R)$ also present qualitative similarities with those of the representative galaxy NGC 5129 and those of ETGs with the most commonly observed shape for $T_X(R)$: $\Sigma_X(R)$ matches the observed profile over many optical effective radii R_e, and $T_X(R)$ reproduces the characteristic bump that peaks at $R = (1 \div 3)R_e$. Inside the peak position, $T_X(R)$ declines toward the center, but the explored models are systematically hotter by $\simeq$30%; possible explanations for this discrepancy are discussed. Interestingly, $\Sigma_X(R)$ and $T_X(R)$ as large as those observed outside $R \simeq R_e$ are reproduced only with significant accretion from a circumgalactic medium, highlighting its importance.

Unified Astronomy Thesaurus concepts: Interstellar medium (847); X-ray astronomy (1810); Galaxy evolution (594); Early-type galaxies (429); Supermassive black holes (1663)

1. Introduction

In the past years, the X-ray properties of the hot interstellar medium (ISM) of early-type galaxies (ETGs) have been deeply investigated, thanks to the data obtained with the Chandra and XMM-Newton observatories (B. Boroson et al. 2011; D.-W. Kim & G. Fabbiano 2015; A.D. Goulding et al. 2016; I. V. Babyk et al. 2018; K. Lakhchaura et al. 2018; N. Islam et al. 2021; E. Nardini et al. 2022 and references therein). In particular, the data of 70 ETGs in the Chandra archive were homogeneously and extensively analyzed, and the resulting hot-gas properties were collected in the Chandra Galaxy Atlas (D.-W. Kim et al. 2019, hereafter K19). Among many products, for each galaxy, this Atlas provides the X-ray luminosity L_X and the average temperature $\langle T_X\rangle$, for the whole galactic extent and within representative radii (e.g., R_e, the optical effective radius, and $5R_e$), and the X-ray surface brightness and temperature profiles $\Sigma_X(R)$ and $T_X(R)$. One major outcome was the recognition that most temperature profiles fit in a "universal" shape (D.-W. Kim et al. 2020, hereafter K20). Except for a set of ETGs (13% of the sample) with $T_X(R)$ monotonically declining outward, for most ETGs (82%), the $T_X(R)$ profile fits in a description that includes a broad bump at intermediate radii, with a maximum T_X located at $(1 \div 3)R_e$, and a decline both inward and outward. Inside a few kiloparsecs, $T_X(R)$ can keep declining down to the innermost observed point, become flat, or show a central increase. The features in this universal profile have been attributed quite naturally to the roles of the environment, for the outer galactic regions, and to active galactic nucleus (AGN) feedback, for the central ones.

On the modeling side, progress has been stimulated by observational results and by advances in hydrodynamical simulations (e.g., E. Choi et al. 2015; L. Ciotti et al. 2017; M. Gaspari et al. 2017; S. Pellegrini et al. 2018; Z. Gan et al. 2019b—hereafter G19b; C. Wang et al. 2019; M. Li et al. 2020; N. Truong et al. 2020; R. Mohapatra et al. 2025). However, no study has so far performed a close comparison between the results obtained for the hot gas by simulations especially designed for realistic ETGs, covering a range of their main properties, and what has been observed for the gas in the X-rays and collected in the large studies mentioned above. We investigate here to what extent the gas properties of the archival Chandra ETGs are reproduced by the modeling of the gas evolution with our high-resolution 2D hydrodynamical code MACER. This modeling includes mass and energy sources from an old stellar population, mechanical and radiative heating from a central AGN, and also important phenomena such as galaxy rotation, star formation, and cosmological inflow from a circumgalactic environment (CGM). The code and the input physics have been developed by L. Ciotti & J. P. Ostriker (2001, 2007, 2012) and

[7] Deceased.

collaborators, with recent major upgrades by Z. Gan et al. (2019a, G19b, 2020). In these simulations, the inner boundaries range from 2.5 to 25 pc, to resolve the Bondi radius; while only performed in 2D, they greatly exceed the spatial resolution available in most cosmological simulations. For a comparison with X-ray observations, we use the set of simulations presented in L. Ciotti et al. (2022, hereafter C22). C22 built realistic dynamical models for the host galaxies, including the possible presence of a group dark matter (DM) halo, for a range of stellar masses and internal stellar kinematics. They used the latest version of the MACER code, which improved in particular the physical treatment of AGN feedback and of star formation and disk instabilities; also considered was the time evolution of the gravitational field of the stellar disk produced by the rotating cooled gas, of the growing central supermassive black hole (SMBH), and of the stellar part of the galaxy due to the mass loss of stars; the SMBH growth and the stellar mass loss also determine the time evolution of the stellar velocity dispersion and rotational velocity fields. The effects of the presence of dust and of a variable metal abundance, whose evolution is separately followed for a number of metal species, were also included (Z. Gan et al. 2020; S. Pellegrini et al. 2020). A preliminary overview of the hot-gas properties of these simulations was given in C22; we focus here on a close comparison of these properties with those observed by Chandra. For the models, we estimate global quantities, such as the X-ray luminosity and the average temperature, computed over the whole galaxy ($L_{\rm X}$ and $\langle T_{\rm X}\rangle$) and within $5R_{\rm e}$ ($L_{\rm X,5}$ and $\langle T_{\rm X,5}\rangle$), and more detailed properties, such as the surface brightness profile $\Sigma_{\rm X}(R)$ and the temperature profile $T_{\rm X}(R)$. We find that the global model properties reproduce well those observed for Chandra ETGs. The $\Sigma_{\rm X}(R)$ and $T_{\rm X}(R)$ profiles are first compared with those of a bright and well-studied galaxy (NGC 5129), which is the prototypical example of the most commonly observed temperature profile (43% of cases) in the classification of $T_{\rm X}(R)$ made by K20 for 60 ETGs. In this class of profile, called "hybrid-bump" (HB), the temperature inside the broad peak keeps declining down to the innermost observed radius. For a few models of the most massive family, which turned out to be structurally similar to NGC 5129, the $\Sigma_{\rm X}(R)$ shape compares well with that of NGC 5129, and their $T_{\rm X}(R)$ show the characteristic observed bump; however, within a few kiloparsecs, the model temperature is larger than that observed by $\simeq$30%. This comparison further indicates the strong importance of CGM accretion for reproducing the outer observed parts of NGC 5129. We then extend the analysis to the $T_{\rm X}(R)$ of all ETGs in the HB class and to the $\Sigma_{\rm X}(R)$ of those ETGs, among these, with optical luminosity similar to that of the successful models; the results obtained from the comparison with NGC 5129 are confirmed and their validity is then extended. In particular, the discrepancy in the behavior of the inner temperature appears to be general; this highlights the need for a wider exploration of the parameters describing AGN accretion and feedback and/or for the inclusion of 3D multiphase effects.

The paper is organized as follows: in Section 2, we briefly describe the models and the simulations; in Section 3, we compare the $L_{\rm X}$, $L_{\rm X,5}$, $\langle T_{\rm X}\rangle$, and $\langle T_{\rm X,5}\rangle$ of the models with those of large samples of ETGs observed with Chandra; in Section 4, we investigate the similarities and differences of the model $\Sigma_{\rm X}(R)$ and $T_{\rm X}(R)$ with those of the representative galaxy NGC 5129 and of ETGs in the HB class; and in Section 5, we discuss the results and present the conclusions.

2. The Galaxy Models

Full descriptions of the structure and dynamical properties of the axisymmetric ellipsoidal galaxy models used in the simulations, the input physics, and the numerical implementation of all physical ingredients are given in C22. Below, we summarize some basic information.

2.1. The Galaxy Structure

The stellar density distribution is an oblate ellipsoidal (W. Jaffe 1983) model of total mass M_*, scale length r_*, and minor-to-major axial ratio q_*:

$$\rho_*(m)=\frac{M_*}{4\pi q_* r_*^3 m^2(1+m)^2},\quad m^2\equiv\frac{R^2}{r_*^2}+\frac{z^2}{q_*^2 r_*^2}. \tag{1}$$

In all the C22 simulations, $q_*=0.7$ is adopted, corresponding to E3 galaxies when seen edge-on. The effective radius of a model observed face-on is $R_{\rm e}^{\rm FO}\simeq 3r_*/4$, and the circularized effective radius of the same model seen edge-on is $R_{\rm e}=\sqrt{q_*}\,R_{\rm e}^{\rm FO}\simeq 0.63r_*$. The stellar distribution is embedded in a galactic DM halo; the stars-plus-DM galaxy density $\rho_{\rm g}$ is a spherical Jaffe distribution of total mass $M_{\rm g}=\mathcal{R}M_*$ and scale length $r_{\rm g}=\xi r_*$, with $\xi\geqslant 1$:

$$\rho_{\rm g}(r)=\frac{M_*\mathcal{R}\xi}{4\pi r_*^3 s^2(\xi+s)^2},\quad s\equiv\frac{r}{r_*}, \tag{2}$$

where $r=\sqrt{R^2+z^2}$ is the spherical radius. C22 adopted $\mathcal{R}=\xi/q_*$, so that $\rho_{\rm DM}=\rho_{\rm g}-\rho_*$ reproduces the Navarro–Frenk–White profile over a large radial range (L. Ciotti et al. 2021); in particular, $\mathcal{R}\simeq 18$ and $\xi\simeq 12.6$ were taken. In order to account for the effects of a group/cluster DM halo on the gas flows, the models are also embedded in a spherically symmetric quasi-isothermal DM halo, of asymptotic circular velocity $v_{\rm h}$, scale length $r_{\rm h}=\xi_{\rm h}r_*$, and density

$$\rho_{\rm h}(r)=\frac{v_{\rm h}^2}{4\pi G r_*^2(\xi_{\rm h}^2+s^2)}. \tag{3}$$

We adopt $\xi_{\rm h}=5$ and $v_{\rm h}^2=2.6\sigma_*^2$, where σ_* is the central stellar velocity dispersion due to $\rho_{\rm g}$ only, so that $\rho_{\rm h}$ is dynamically important only outside several $R_{\rm e}$. Finally, an SMBH of initial mass $M_{\rm BH}=\mu(0)M_*=10^{-3}M_*$ is added at the center of the galaxy; this provides a time-evolving potential $\phi_{\rm BH}(r,t)=-GM_*\mu(t)/r$, the consequence of SMBH accretion.

C22 adopted three values for the initial stellar mass—i.e., $M_*=1.54\times10^{11}M_\odot$, $3.35\times10^{11}M_\odot$, and $7.80\times10^{11}M_\odot$—that correspond to the LM, MM, and HM families of models. For all models, the dark mass fraction $M_{\rm DM}(r)/M_{\rm g}(r)$ is $\simeq$0.52 for $r=R_{\rm e}$ and $\simeq$0.64 for $r=2R_{\rm e}$.

The stellar velocity dispersion and the ordered velocity field $\overline{v_\varphi}$ are determined as described in C22. The equal vertical and radial components of the stellar velocity dispersion σ_* and the quantity $\Delta_*=\overline{v_\varphi}^2+\sigma_\varphi^2-\sigma_*^2$ (where σ_φ is the azimuthal dispersion) are obtained from the Jeans equations. Then, $\overline{v_\varphi}$ is

Table 1
Structural Properties of the Models

Model Family	L_K ($10^{11}\,L_{K,\odot}$) (1)	M_* ($10^{11}\,M_\odot$) (2)	r_* (kpc) (3)	R_e (kpc) (4)	$\sigma_*(0)$ (km s^{-1}) (5)	v_h (km s^{-1}) (6)
LM	1.30	1.54	7.33	4.57	223	360
MM	2.65	3.35	11.29	7.04	265	427
HM	5.62	7.80	18.94	11.80	312	504

Notes. For each model family, the columns are as follows. Column (1): the galaxy luminosity in the K band. Column (2): the initial stellar mass. Column (3): the scale length of the stellar distribution (Equation (1)). Column (4): the edge-on circularized effective radius. Column (5): the central stellar velocity dispersion in absence of the SMBH. Column (6): the asymptotic circular velocity of the quasi-isothermal DM halo (Equation (3)). The models were built to lie on the fundamental plane of ETGs.

given by a generalized C. Satoh (1980) k-decomposition:

$$\overline{v_\varphi} = k\,\sqrt{\Delta_*}, \quad \sigma_\varphi{}^2 = \sigma_*^2 + (1-k^2)\Delta_*. \tag{4}$$

For each galaxy mass M_*, three types of rotation fields were implemented: nonrotating ($k = 0$) galaxies, where the stellar flattening q_* is totally produced by σ_φ; fast-rotating, isotropic ($k = 1$) galaxies, with the flattening totally supported by ordered rotation; and galaxies with a spatially dependent Satoh parameter:

$$k_e(r) = e^{-r/R_e}. \tag{5}$$

In this way, a total of nine galaxy models were studied. The main properties of the three families of models are summarized in Table 1, and the nine models are listed in Table 2.

2.2. The Input Physics and the Hydrodynamical Simulations

The input physics of the models (e.g., AGN feedback, star formation, and disk instabilities) and the numerical treatment of the hydrodynamical equations are described in Section 3 of C22. Here, we recall their main characteristics.

The mass source terms for the gas flows are given by the mass losses from evolved stars, type Ia supernova (SN Ia) explosions, and type II supernovae (SNe II) from the new stars formed (see Appendix B in G19b as well as L. Ciotti & J. P. Ostriker 2012; S. Pellegrini 2012) and by cosmological accretion from the CGM. Stellar mass losses inject gas with a time decreasing rate $\dot{\rho} = (\dot{M}_*/M_*)\rho_*$, where ρ is the gas density (see Figure 1). Over ≈10 Gyr, this mass injection term sums up to a total gas mass of $\simeq 0.1 M_*$. Figure 1 also shows the mass input rate from SN Ia explosions ($\dot{M}_{\rm Ia}$). Following G19b, the time-dependent rate of mass accretion from the CGM is $\dot{M}_{\rm CGM} \propto t\,e^{-t^2/t_0^2}$, which approximates the results of cosmological zoom-in simulations for massive ellipticals; C22 adopted $t_0 = 9$ Gyr, and the proportionality constant in the formula such that the total accreted mass from the CGM between 2 and 12 Gyr is $\simeq 0.4 M_*$. The mass accretion from the CGM is imposed at the outer boundary (250 kpc) of the numerical grid, and the CGM mass flux is weighted by a $\sin^2\theta = R^2/r^2$ angular dependence, so that most of the CGM is injected near the equatorial plane.

The various source terms inject into the galaxy also momentum and internal and kinetic energy (Section 3 of C22). In particular, the stellar kinematical properties enter the thermalization term in the energy equation according to Equation (17) of C22 and the momentum equation through Equation (18) of C22. In the rotating models, the momentum injection leads to the formation of the cold gaseous equatorial disk, a place of star formation. The CGM inflow also injects momentum and energy: the CGM injection velocity is half of the freefall velocity from infinity (Equation (19) of C22), and the internal energy of the infalling gas is such that its sound velocity equals the injection velocity (G19b).

Star formation in the cold gaseous disk, which forms in rotating models, is implemented as a result of Toomre instability plus physically based conditions of gas density and temperature, as described in Equations (20)–(21) of C22. Star formation is also allowed to occur everywhere in the galaxy, provided that: (1) the gas temperature falls below 4×10^4 K; and (2) the gas number density is higher than $10^5\,{\rm cm}^{-3}$. Under such conditions, the timescale of star formation is given by $\max(\tau_{\rm cool}, \tau_{\rm dyn})$, with $\tau_{\rm cool}$ being the standard cooling time and $\tau_{\rm dyn}$ as defined in Equations (23) and (23) of G19b. The adopted initial mass function (IMF) is

Table 2
X-Ray Model Properties at a Galaxy Age of 10 Gyr

Model Name (1)	L_X (10^{40} erg s^{-1}) (2)	$\langle T_{X,5}\rangle$ (10^7 K) (3)	$\langle T_X\rangle$ (10^7 K) (4)
LM_0	8.09	0.59	0.59
LM_k	3.06	0.76	0.60
LM_1	2.24	0.88	0.61
MM_0	44.9	1.09	0.78
MM_k	14.6	0.99	0.76
MM_1	10.1	1.01	0.74
HM_0	243	1.31	0.97
HM_k	80.2	1.18	0.96
HM_1	55.0	1.20	0.96
$HM_k^{\rm new}$	57.0	1.24	0.98
$HM_k^{\rm noCGM}$	3.22	0.92	0.92

Note. Column (1): model names—for each model mass (LM, MM, or HM), the subscript indicates the type of azimuthal stellar motion, as described in Section 2.1; in order of increasing importance of rotational support, "0" means no ordered rotation ($k = 0$), "k" indicates the exponentially declining rotation $k_e(r)$ in Equation (5), and "1" is the isotropic rotator ($k = 1$). Column (2): the total luminosity L_X of the hot gas in the 0.3–8 keV energy band. Column (3): the 0.3–8 keV average temperature, computed as detailed in Appendix A.3, for an aperture of $5R_e$. Column (4): the 0.3–8 keV average temperature computed for the whole galaxy. The first nine models were run by C22, while the last two have been run for the discussion in Section 4.

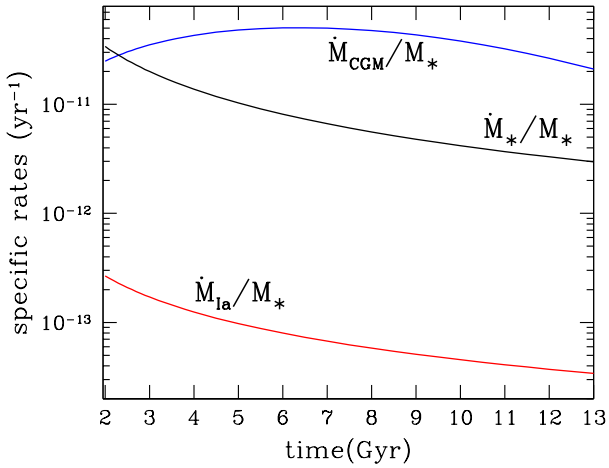

Figure 1. The rates of mass input to the ISM described in Section 2.2, each normalized to M_*. The aging stellar population inputs are $\dot{M}_*$ (in black) and $\dot{M}_{Ia}$ (in red); the CGM infall $\dot{M}_{CGM}$ (in blue) is parameterized as in C22.

such that ≃60% of the mass of newly formed stars is in stars with mass $>8M_\odot$ that explode as SNe II on a timescale of $\approx 2 \times 10^7$ yr and inject their mass into the ISM; the motivation for this IMF is discussed in C22.

Finally, the implementation of AGN feedback in its radiative and mechanical (momentum and kinetic energy) components, where the latter is due to AGN winds, is described in Section 2.7 of G19b, with the small modifications illustrated in Section 3 of C22. AGN feedback is self-consistently triggered by the accretion of low-angular-momentum gas, along the polar direction, and of recurrent discharges of gas on the central SMBH due to the Toomre instability in the cold rotating disk. The implementation of this second accretion channel is done via the modeling described in Section 3 of C22.

The Eulerian hydrodynamical equations are solved with the high-resolution grid code MACER, based on the Athena++ code (J. M. Stone et al. 2020), in spherical coordinates (r, θ), assuming axisymmetry. More details of the code and the numerical scheme of integration are given in Section 3.1 of C22. The innermost grid point is placed at 25 pc from the center, the outermost at 250 kpc. The age of the galaxy at the beginning of the simulation is 2 Gyr, so that the initial phases of galaxy formation are terminated, and the flow evolution is followed for 11 Gyr; in the central regions, during outbursts, the fluctuations are followed with a temporal resolution as short as $\simeq 10^3$ yr.

3. X-Ray Luminosities and Temperatures of the Hot Gas

We present here a first test for the viability of the implementation of the input physics in the models: the agreement (or not) with observed values of their global X-ray properties, such as the hot-gas luminosity L_X and its average temperature $\langle T_X \rangle$. For this test, we look at the distribution of the models in diagnostic planes as $L_X - L_K$ and $L_X - \langle T_X \rangle$, where L_K is the K-band galaxy luminosity. To determine model quantities analogous to those measured in the X-rays, we proceeded as follows (more details are given in Appendix A). The X-ray emissivity in the 0.3–8 keV energy band, considering the possibility of absorption by intervening cold gas within the galaxy (e.g., due to the cold disk), was integrated along the line of sight, for an edge-on view of the galaxy; the result was a surface brightness map Σ_X, which was integrated in the image plane to compute the total L_X, and that within a cylinder of radius equal to $5R_e$ and its axis along the line of sight, $L_{X,5}$ (Equation (A10)); the circularized surface brightness profile $\Sigma_X(R)$ was determined as an angle-averaged quantity over an annulus centered at R (Equation (A12)). The average temperatures were derived first by performing a projection along the line of sight of the gas temperature weighted with the X-ray emissivity, including again the possibility of intrinsic absorption (Equation (A11)); from the temperature map so obtained, we evaluated the circularized temperature profile $T_X(R)$ (Equation (A12)); weighting $T_X(R)$ with $\Sigma_X(R)$, we computed the average temperature $\langle T_X \rangle(R)$ within the radius R in the image plane[8] (Equation (A13)). In the following, we consider the average temperatures $\langle T_{X,5} \rangle$, within an aperture of radius $5R_e$, and $\langle T_X \rangle$ for the whole galactic image.

Figure 2 shows the position of the models in the $L_X - L_K$, $L_X - \sigma_0$ (the central stellar velocity dispersion), $\langle T_{X,5} \rangle - L_K$, and $\langle T_{X,5} \rangle - \sigma_0$ planes. The red symbols indicate the nine models in C22, and the green symbols indicate the two additional models discussed in Section 4, at a representative galaxy age of 10 Gyr (Table 2).[9] Each model can be identified from its L_K (in Table 1), its L_X (in Table 2), and its rotational properties, which are also specified in the figure. The observed quantities in Figure 2 derive from Chandra pointings: L_X is the 0.3–8 keV hot-gas luminosity, measured from within the largest available radius (D.-W. Kim & G. Fabbiano 2015; K19); $\langle T_{X,5} \rangle$ is the average luminosity-weighted temperature within a circle of radius $5R_e$ or, when not available (13 cases), within a smaller radius (from K19). In all four panels, the distribution of the models falls within that of observed ETGs and also reproduces the general observed trends. In the top left panel ($L_X - L_K$), the model L_X at each L_K decreases for an increasing amount of ordered rotation; this confirms previous findings, also obtained with different galactic structures and different codes (i.e., A. Negri et al. 2014a, 2014b). The trend is explained by the tendency of rotating flows to induce gas cooling in the central regions; in addition, more gas mass can be ejected as the gas centrifugal support increases, thus the overall effect of rotation is to produce more cold gas and less hot ISM (see Table 2 in C22 as well as S. Posacki et al. 2013). A trend in this sense has been also observed: flatter galaxies, which tend to rotate more, show on average lower L_X (P. B. Eskridge et al. 1995; M. Sarzi et al. 2013; A. Juranova et al. 2020). In the bottom left panel ($L_X - \sigma_0$), $\sigma_*(0)$ in Table 1 is used as a proxy for the projected σ_0 of the models; these fall within the observed distribution and follow its general trend. We note that this plot is not just a replication of the $L_X - L_K$ plane, because even though L_K and σ_0 correlate through the Faber–Jackson relation, they do so with a large scatter.

The right panels in Figure 2 show the $\langle T_{X,5} \rangle$ versus L_K and $\langle T_{X,5} \rangle$ versus σ_0 planes, for the set of ETGs with $\langle T_{X,5} \rangle$ available in the Chandra Galaxy Atlas (K19). For these panels, we adopted a temperature within an aperture of $5R_e$, instead of the global $\langle T_X \rangle$, because a temperature averaged over a smaller

[8] The average temperatures and the $T_X(R)$ profiles obtained with this procedure are emission-weighted quantities, as are, with good approximation, the observed temperatures used for comparison in this work; see K19 and N. Truong et al. (2020).

[9] C22 report L_X from a spherical volume of $r < 5R_e$, at an age of 13.7 Gyr, in their Table 2; also, there, the L_X of model HM_0 should read 129 instead of the reported 12.9, due to a typo.

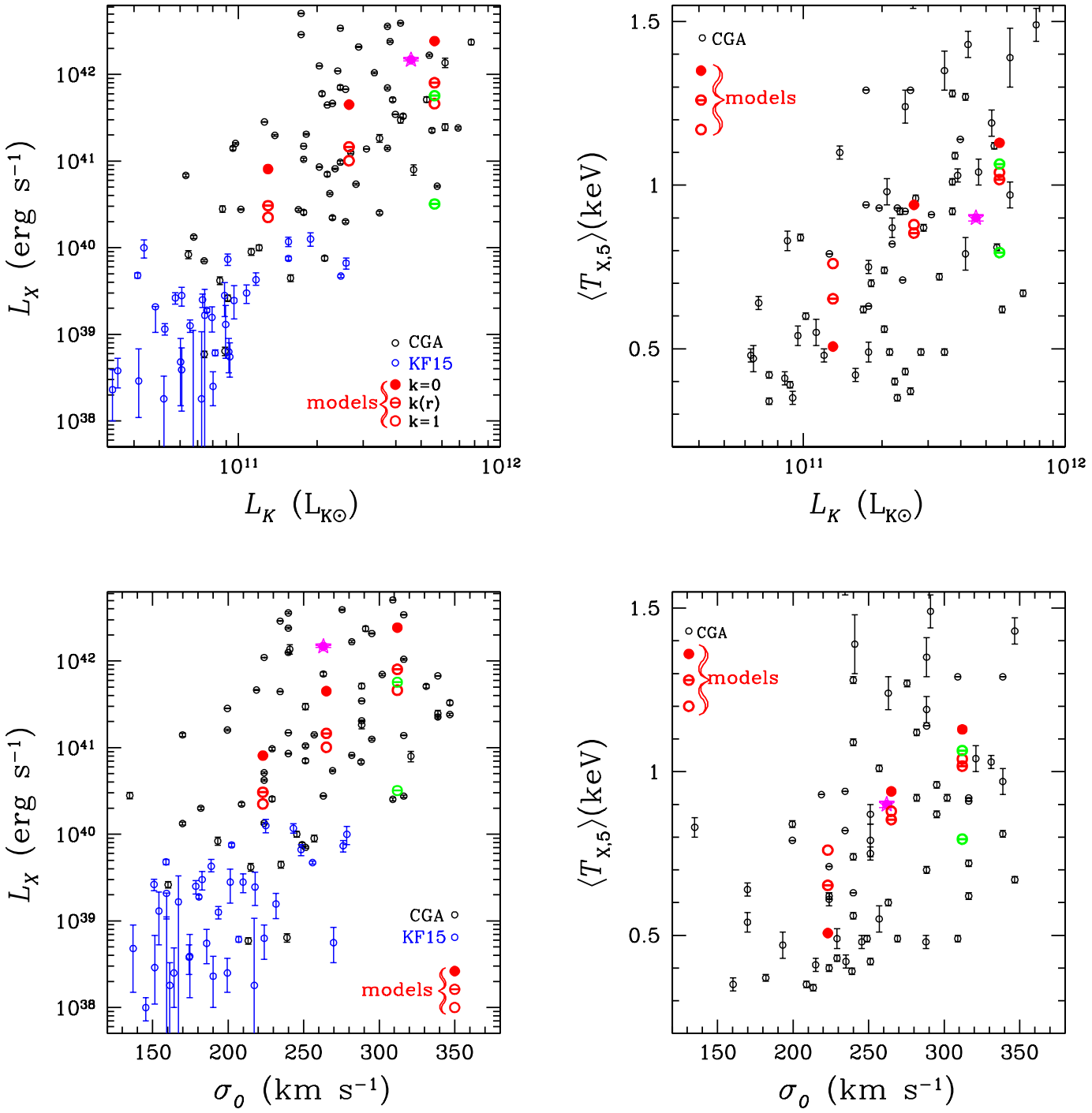

Figure 2. X-ray properties of the models in Table 2 compared with the corresponding properties for two samples: the ETGs in the Chandra Galaxy Atlas (K19—"CGA" in the legend) and those in the ATLAS^{3D} sample observed with Chandra (D.-W. Kim & G. Fabbiano 2015—"KF15" in the legend). Upper left: the total 0.3–8 keV L_X vs. the K-band galactic luminosity L_K. Upper right: the 0.3–8 keV average temperature within $5R_e$, $\langle T_{X,5}\rangle$ vs. L_K, for the models and CGA galaxies. Lower left: L_X vs. the central stellar velocity dispersion σ_0; for observed galaxies, the σ_0 come from KF15, K20, and I. V. Babyk et al. (2018); for the models, σ_0 is $\sigma_*(0)$ in Table 1. Lower right: the same $\langle T_{X,5}\rangle$ as in the upper right panel vs. σ_0. See Section 3 for more details. In all panels, the pink star shows the galaxy NGC 5129, and the two green symbols show the two additional models HM$_k^{new}$ and HM$_k^{noCGM}$ in Table 2, discussed in Section 4.

region is more sensitive to the model properties, as the rotational support; instead, $\langle T_X\rangle$ depends almost exclusively on the galaxy mass and is very similar for models of the same mass (see Table 2). At variance with what happens for L_X, which decreases with increasing rotation at each L_K (and σ_0), here the relation between rotation and $\langle T_{X,5}\rangle$ depends on the galaxy mass: in the MM and HM models, $\langle T_{X,5}\rangle$ is lower when rotation is present, because the cold-disk formation leaves a lower hot-gas density in the central (typically hotter) region (see also Section 4); in the LM models, instead, rotation is more effective in favoring the development of winds, which are hotter than inflowing gas, and thus the opposite trend of $\langle T_{X,5}\rangle$ with rotation is established (see also A. Negri et al. 2014b).

Another common diagnostic diagram is the L_X–$\langle T_X\rangle$ plane (e.g., D.-W. Kim & G. Fabbiano 2015; A.D. Goulding et al. 2016;

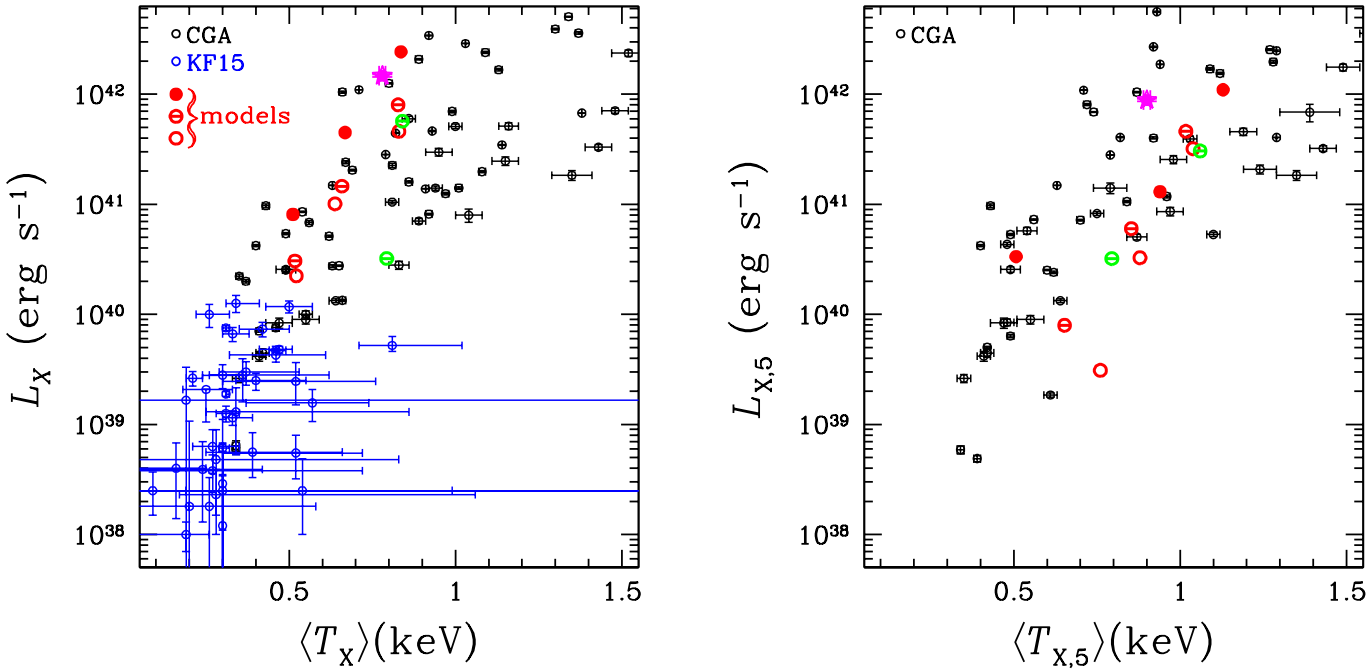

Figure 3. Left panel: L_X vs. $\langle T_X \rangle$ for the models in Table 2 and observed ETGs; references for the observed quantities, symbols, and meanings of the legend are the same as in the upper left panel of Figure 2. Right panel: $L_{X,5}$ vs. $\langle T_{X,5} \rangle$ for the models in Table 2 and observed ETGs from K19 only. The pink star shows NGC 5129, and the two green symbols show the two additional models HM_k^{new} and HM_k^{noCGM}, discussed in Section 4.

I. V. Babyk et al. 2018), shown here in the left panel of Figure 3; as for L_X, the observed $\langle T_X \rangle$ also derives from the largest extraction radius available. In this plane, the positions of the models fall within those of the observed ETGs; each family of LM, MM, and HM models is located along an almost vertical column of red (and green) points, since $\langle T_X \rangle$ depends mostly on the galaxy mass. Except for one green point, however, the models tend to reside in the region of the more X-ray-luminous ETGs, at a fixed $\langle T_X \rangle$, or of the lower $\langle T_X \rangle$, at a fixed L_X. To further investigate this point, we made closer the comparison between models and observations, by plotting strictly matching quantities in terms of the extraction region for the computation of luminosity and average temperature. The right panel of Figure 3 thus shows $L_{X,5}$ versus $\langle T_{X,5} \rangle$; here, only those ETGs on the left, for which these quantities are available in the Chandra Galaxy Atlas (K19), are plotted. In the right panel, the models have moved toward larger temperatures ($\langle T_{X,5} \rangle > \langle T_X \rangle$ for most of them; Table 2), while the distribution of ETGs overall has not changed much (for a number of them, $\langle T_X \rangle$ in the left panel is already estimated at or close to $5R_e$). Also, $\langle T_{X,5} \rangle$ is more different than $\langle T_X \rangle$ for models of the same mass,[10] so the models' positions are more spread over the plane. The result is that now the models fall within, and cover well, the range of observed values. We note finally that the green point with the lower L_X in Figure 3 (and Figure 2 as well) is a model equal to HM_k but evolved without CGM accretion (model HM_k^{noCGM} in Table 2). Its L_X is much lower than that of HM_k, indicating how this kind of accretion can produce a large variation in L_X, at fixed L_K. Its $\langle T_X \rangle$ is equal to $\langle T_{X,5} \rangle$, due to its peaked $\Sigma_X(R)$. This model will be considered further in Section 4.

[10] The difference between $\langle T_{X,5} \rangle$ and $\langle T_X \rangle$, like that between $L_{X,5}$ and L_X, depends of course on the shapes of $\Sigma_X(R)$ and $T_X(R)$ (Equation (A13)); for example, the difference is lower for a more peaked $\Sigma_X(R)$, which reduces the importance of the galaxy regions outside $5R_e$.

In conclusion, the L_X, $L_{X,5}$, $\langle T_X \rangle$, and $\langle T_{X,5} \rangle$ of the models are found within the observed range, and also their trends with L_K and σ_0 are satisfactory: more massive galaxies are more X-ray-luminous and hotter than less massive systems—a well-known manifestation of the larger binding energy per unit gas mass in larger galaxies (as indicated, e.g., by the Faber–Jackson relation). Moreover, less rapidly rotating systems are more X-ray-luminous than more rotating ones of the same mass, a trend also possibly present in the observations. A tendency for the models to occupy the upper envelope of the observed L_X distribution, at fixed $\langle T_X \rangle$, disappears when considering $L_{X,5}$ and $\langle T_{X,5} \rangle$.

4. X-Ray Surface Brightness and Temperature Profiles

Here, we explore how the brightness profile $\Sigma_X(R)$ and the temperature profile $T_X(R)$ of the models compare with those observed; for this purpose, these profiles were computed in a way to obtain quantities analogous to those measured (Section 3; Appendix A). Indeed, global X-ray properties that are even consistent with observations could be associated with $\Sigma_X(R)$ and $T_X(R)$ that are different from those observed; thus, this study can provide additional information on the performance of the models and on the possible need for modifications in the input physics. Since the simulations of C22 were not designed to reproduce a specific ETG, we first select a representative galaxy in the Chandra Galaxy Atlas and carry out a comparison with its $\Sigma_X(R)$ and $T_X(R)$, recalling that the analysis can sometimes only be qualitative. Next, in Section 4.1, we extend the comparison to more ETGs in this Atlas.

As a representative galaxy, we selected NGC 5129, an X-ray-bright ETG with an extended hot halo. Its $T_X(R)$ profile fits in the universal shape and in particular is the prototypical example of the most commonly observed type of profile—the HB one (K20; see Section 1). At a distance of 103 Mpc, NGC

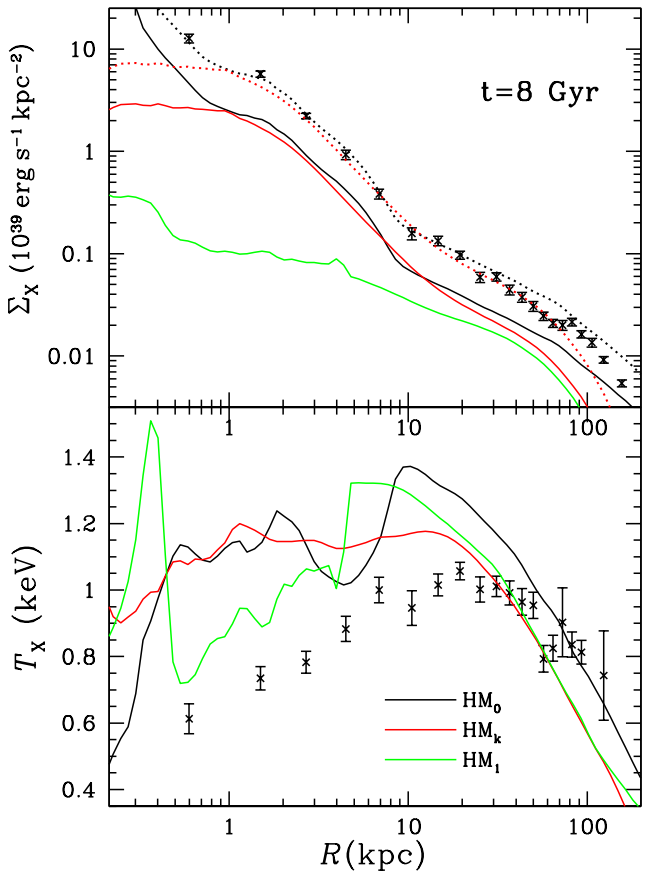

Figure 4. The 0.3–8 keV circularized surface brightness profiles $\Sigma_X(R)$ (upper panel) and temperature profiles $T_X(R)$ (lower panel), at an age of 8 Gyr, for the three HM models of C22 (Table 2), shown with solid lines of different colors (as specified in the legend of the lower panel); with the same colors, the dotted lines show the brightness profiles of the HM$_0$ and HM$_k$ models scaled up by a factor of 2.5 (Section 4). The corresponding profiles for NGC 5129 are shown by the black symbols with error bars (from K19).

5129 is a moderately rotating E3–E4 galaxy, with $L_K = 4.6 \times 10^{11} L_{\odot,K}$, a stellar mass of $M_* = 7.2 \times 10^{11} M_\odot$, and $R_e = 14$ kpc (M. Veale et al. 2017)—all properties that make it similar to the galaxies of the HM family. NGC 5129 is also the dominant galaxy in a poor galaxy group, and its estimated age within $R_e/8$ is 7.4 Gyr (M. Gu et al. 2022). Its L_X, $L_{X,5}$, $\langle T_{X,5}\rangle$, and $\langle T_X\rangle$ are shown in Figures 2 and 3 with the pink star. NGC 5129 was also studied in the X-rays by H. J. Eckmiller et al. (2011), V. Bharadwaj et al. (2014), and J. M. Nugent et al. (2020). All these studies found a central positive gradient in the temperature profile, a peak of $kT \simeq 1.1$ keV at $R \simeq 20$ kpc, and then a decline out to $R \approx 200$ kpc. The most spatially detailed $\Sigma_X(R)$ and $T_X(R)$ profiles are those determined from Chandra data by K19, and we consider them in the following.

For the three HM models, Figure 4 shows the circularized $\Sigma_X(R)$ and $T_X(R)$ profiles, together with those of NGC 5129; here, R is the distance from the galactic center in the X-ray image, and the models are viewed edge-on (Appendix A.3). The model profiles refer to an age of 8 Gyr. It is apparent how the Σ_X shape becomes more similar to that of NGC 5129 when decreasing the amount of stellar ordered rotation (i.e., going from the green to the red to the black solid lines); rotation tends to make the brightness profile flat within $R \simeq 10$ kpc, a result in line with those obtained from past simulations (F. Brighenti et al. 2009; A. Negri et al. 2014a). In order to compare more closely the $\Sigma_X(R)$ of the nonrotating HM$_0$ model with that of NGC 5129, we scaled its $\Sigma_X(R)$ up by a factor of $\simeq$2.5 and obtained the black dotted line in Figure 4. The scaled Σ_X shows a good match with that observed; however, it seems to be increasing too steeply at the center ($R \lesssim 500$ pc), and it keeps above the observed profile for $R \gtrsim 30$ kpc. The same scaling operation applied to the $\Sigma_X(R)$ of the mildly rotating HM$_k$ (the red dotted line in Figure 4) also provides a good match with observations over a radial range from $\simeq$1 to $\simeq$70 kpc; outside this range, it is lower than observed. The $\Sigma_X(R)$ of the highly rotating HM$_1$ model is too discrepant and no scaling was tried. We note that the Σ_X shapes remain similar during the last Gyr of evolution, for each of the HM$_0$, HM$_k$, and HM$_1$ models, therefore the choice of the age is not crucial for the above conclusions. From a physical point of view, the scaling of Σ_X by a factor of $\simeq$2.5 can be produced by a uniform increase of the gas density by $\simeq$50%—a variation that is not unreasonable to hypothesize for NGC 5129, considering that HM models were not tailored on it. Σ_X instead would not scale similarly for a uniform temperature variation, because the 0.3–8 keV emissivity is weakly dependent on the temperature when it varies in the range of $\simeq$0.3–1.2 keV.

The lower panel of Figure 4 shows the temperature profiles of the three HM models, at the same epoch of 8 Gyr. In the outer galactic region ($R \gtrsim 30$ kpc), $T_X(R)$ has the correct shape and range of values, while it is different from that observed inside $R \simeq 20$ kpc. In particular, the observed bump is absent, and all models show larger temperatures. Model HM$_0$ shows the largest disagreement with the NGC 5129 temperature profile, being almost everywhere too hot. Of the two remaining models, HM$_1$ shows unobserved temperature fluctuations, while HM$_k$ seems the least discrepant with observations. Can modifications of the HM$_k$ model give a temperature profile that better reproduces the observed one and at the same time maintain the good agreement of $\Sigma_X(R)$ with that of NGC 5129? In order to investigate this aspect, we explored some changes in various parameters of the input physics, while keeping the same galaxy structure and rotation properties of HM$_k$. Given the computational time required by the simulations, a full parameter space exploration is prohibitive. Some experiments involving changes in the AGN feedback parameters (such as the AGN wind opening angle and velocity) or in the energy injected by SNe II from star formation in the central regions did not produce improvements. Instead, changes in the implementation of the environmental accretion produced variations in $T_X(R)$ in the sought directions. In particular, this was the case for an increase of the CGM accretion velocity imposed at the outer boundary by a factor of 1.5 (from 0.5 to 0.75 of the galaxy freefall velocity; see Section 2.2), with the CGM mass inflow $\dot{M}_{CGM}$ kept the same. The L_X, $L_{X,5}$, $\langle T_X\rangle$, and $\langle T_{X,5}\rangle$ of this variant of HM$_k$ (hereafter HM$_k^{new}$) are shown in Figures 2 and 3 by the green points with the larger luminosity and temperature values; reassuringly, they still fall within the observed range. Figure 5 (left panel) shows $\Sigma_X(R)$ and $T_X(R)$ of HM$_k^{new}$, at three different epochs, close to the age of NGC 5129. Similar to what was done for HM$_0$ and HM$_k$, here $\Sigma_X(R)$ is upscaled by a factor of $\simeq$3. The agreement of the rescaled $\Sigma_X(R)$ profiles with the observed one is still good: the observed shape between $R = 1$ and $R = 10$ kpc is well reproduced, and also its flattenings inside $R = 1$ kpc and outside $R = 10$ kpc. It is remarkable that the L_X

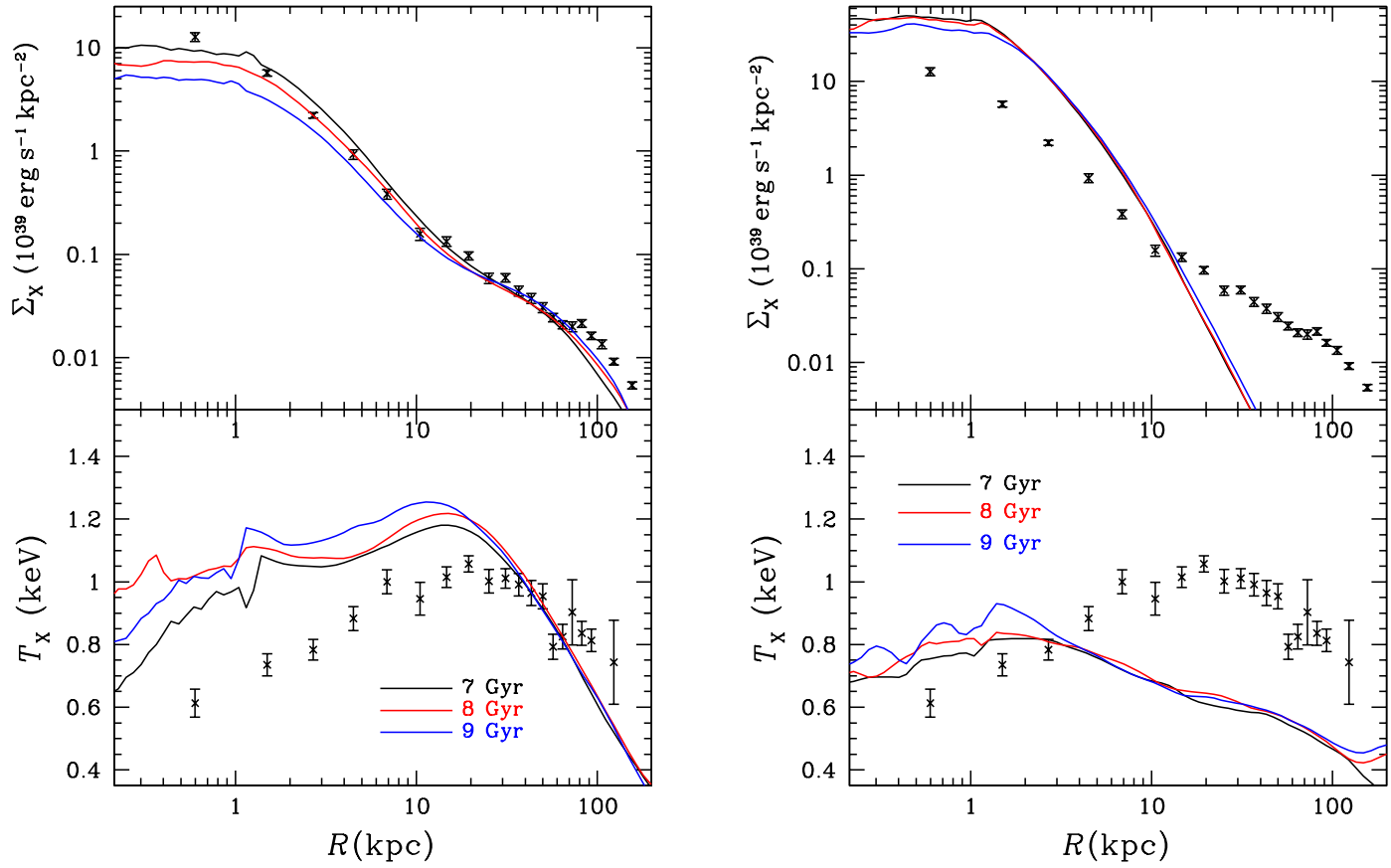

Figure 5. Left panels: model HM_k^{new}, at three representative epochs, compared with NGC 5129 (the points with error bars; from K19). The model $\Sigma_X(R)$ have been scaled up by a factor of ≃3 to match the profile of NGC 5129 (Section 4); notice how the model profiles reproduce the change of slope outside $R \simeq 10$ kpc. Right panels: model HM_k^{noCGM}, at the same epochs as in the left panels, compared with NGC 5129; this model is equal to the HM_k models but has been evolved without CGM mass accretion. The model $\Sigma_X(R)$ has been rescaled, as for HM_k^{new}, for plotting purposes (Section 4). The $T_X(R)$ profiles of HM_k^{noCGM}, in the outer region, are lower than observed, proving that CGM accretion is here fundamental to shaping the temperature profile.

value resulting for the scaled model is close to that measured for NGC 5129 from its spectrum, i.e., $L_X = 1.48 \times 10^{42}$ erg s^{-1} within $R = 145$ kpc (K19). The HM_k^{new} temperature profile is less spatially fluctuating and shows a better defined and smoother bump, with respect to that of HM_k; the presence and location of this bump, which extends from 8 to 20 kpc, make $T_X(R)$ of HM_k^{new} closer to the observed one. Outside $R \simeq 20$ kpc, the decline in $T_X(R)$ and its values match those observed. Inside $R \simeq 20$ kpc, however, the slope of $T_X(R)$ is now similar to that observed, but the $T_X(R)$ values remain larger by ≃30%. Note that some residual uncertainties, produced by the use of different emission models and atomic data, might still be present in the measured temperature profile. We discuss further possible origins of the discrepancy in temperature in Section 5.

The importance of CGM accretion in determining the brightness and temperature profiles is especially revealed by an experiment where it is suppressed. This model (HM_k^{noCGM}) is shown in Figures 2 and 3 by the green points with the lower luminosities and temperatures. L_X, $L_{X,5}$, $\langle T_{X,5}\rangle$, and $\langle T_X\rangle$ are still within the observed range, though on the lower side of the distribution of values. The L_X of HM_k^{noCGM} is much lower than that of the other HM models—a combined consequence of the absence of CGM accretion and of the greater ease for the galaxy degassing, due to the lack of a confining CGM. Figure 5 (right panels) shows $\Sigma_X(R)$ and $T_X(R)$ of HM_k^{noCGM}. The $\Sigma_X(R)$ profile is completely different from that of NGC 5129: it is far more peaked in the central galactic region and too steeply declining outside $R \simeq 10$ kpc (for plotting purposes, Σ_X has been rescaled to reach the luminosity of NGC 5129, which requires a factor of ≃40, which is of course far larger than for the HM models with CGM accretion). The temperature is decreased at all radii, and the $T_X(R)$ profile takes a flatter shape: it lacks the characteristic bump feature, and a much less pronounced maximum is present closer to the galactic center (at $R \simeq$ (1–2) kpc). The lower temperature values, and in particular the steady decline in $T_X(R)$ outside $R = 2$–3 kpc, are a consequence of the missing confinement effect of the CGM and the lack of gravitational compression work done by accretion. Indeed, there is observational evidence that the shape of $T_X(R)$ in the outer galactic regions is sensitive to the presence of an intracluster or intragroup medium (e.g., K20). Finally, notwithstanding the decrease in T_X at all radii, at the center the temperature of HM_k^{noCGM} remains slightly larger than observed.

4.1. Comparison with More Galaxies in the Chandra Galaxy Atlas

The detailed comparison in the previous Section 4 concerned an ETG representative of the HB class of temperature profiles—the most commonly observed one. We extend here the comparison of the most successful model for reproducing NGC 5129 (HM_k^{new}) to more ETGs of the HB

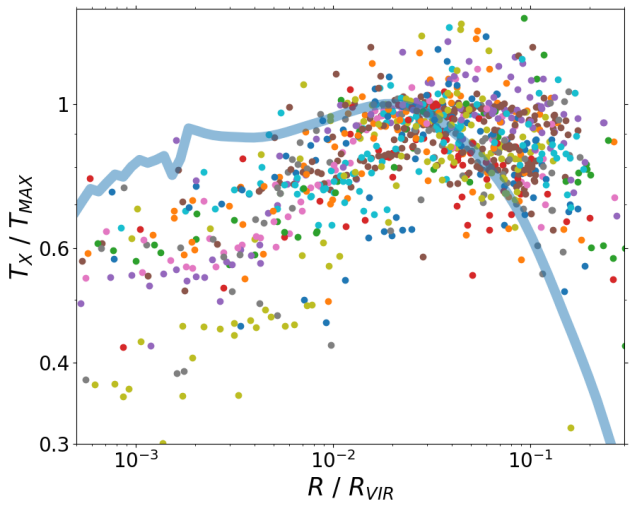

Figure 6. Model HM_k^{new} at 7 Gyr (light blue solid line) compared with the temperature data for ETGs of the HB class (26 galaxies) and of the double-break class (four galaxies); each galaxy is plotted with a different color. The temperatures are scaled by T_{MAX}, the maximum temperature value, and the galactocentric distances to R_{VIR}, the virial radius, both determined as detailed in Section 4.1. This plot is based on Figure 6 in K20, from where the observed temperatures are taken.

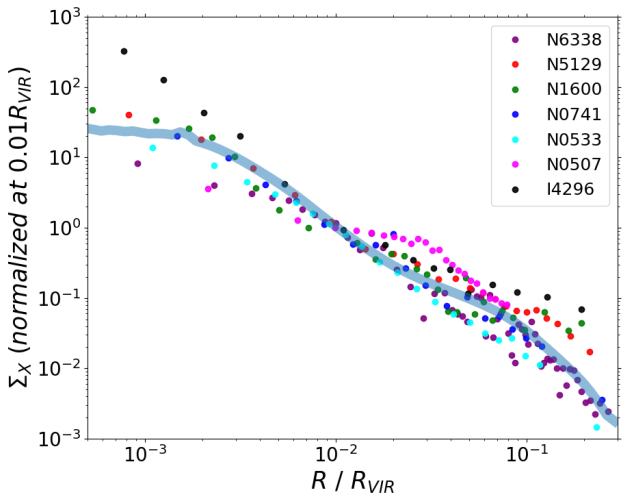

Figure 7. Model HM_k^{new} at 7 Gyr (light blue solid line) compared with the surface brightness profiles for 7 ETGs with L_K similar to that of HM models (from K19); the names of these galaxies are reported in the upper right legend. The galactocentric distances are scaled by the respective R_{VIR}, and each $\Sigma_X(R)$ is scaled by its value at $0.01R_{VIR}$. See Section 4.1 for more details.

class. This analysis will strengthen or weaken the significance of the results in Section 4.

Figure 6 shows the temperature profile of HM_k^{new}, together with all those classified as the HB (26 ETGs) and double-break[11] (four ETGs) types by K20; the plot is based on Figure 6 in K20. For a proper comparison, each profile is scaled by its T_{MAX}, the maximum temperature of the best-fitting model reproducing it; the radial scale is normalized for each galaxy to its fiducial virial radius R_{VIR}, determined from the average hot-gas temperature, as in the relation from S. F. Helsdon & T. J. Ponman (2003) used by K20. For HM_k^{new}, this relation gives $R_{VIR} = 0.75$ Mpc, close to $R_{VIR} = 0.73$ Mpc of NGC 5129 (K20). The model, plotted with a light blue curve, falls within the distribution of observed points and, even after the scaling that is not applied in Figures 4 and 5, again shows a bump located in the radial range where it appears for observed ETGs. Within $R \approx 0.004R_{VIR}$, the observed temperatures show a large scatter, and the model lies on the upper envelope of the distribution of points. Therefore, the result of a temperature larger than observed in the central region, evidenced by the comparison with NGC 5129, cannot be discarded as being due to some peculiar properties of this galaxy but rather looks like a feature of the numerical model. We note that different estimates for the value of R_{VIR} produce a horizontal shift of the $T_X(R)$ profile and, in particular, a reduction of R_{VIR} for the model would shift its $T_X(R)$ to the right, alleviating the discrepancy; however, a discrepancy was also present in the analysis of Section 4 (in Figures 4 and 5), where the radial scale is fixed, and the comparison of a model with observations is direct.

A similar comparison of $\Sigma_X(R)$ of HM_k^{new} with that of ETGs in the HB class is more difficult. In fact, while the temperature profiles could be classified into specific types, the analog classification for $\Sigma_X(R)$ is not available; indeed, the brightness profiles seem to vary more than the temperature ones. Also, it is more uncertain how to compare them for a large sample, because the choice of a proper scaling is not straightforward; for example, the brightness peak lies at the center and then suffers from observation-dependent biases (such as galaxy distance and exposure, etc.). For these reasons, we first selected those ETGs in K20 with L_K similar to that of the HM models—i.e., in a range from 4.2 to $7 \times 10^{11} L_{K,\odot}$. Of the 10 resulting galaxies, all turned out to belong to the HB temperature class, except for one that was excluded. Two ETGs with a poorly known brightness profile in the Chandra Galaxy Atlas (K19) were further excluded. The remaining seven galaxies are shown in Figure 7, together with model HM_k^{new} in light blue; here, the galactocentric distances R are measured again in units of R_{VIR}, and $\Sigma_X(R)$ of each galaxy is normalized by its value at the intermediate radius $0.01R_{VIR}$. The model compares well with observations over the whole radial range and represents a reasonable average for the normalized $\Sigma_X(R)$ profiles. Two galaxies stand out for deviations from the general behavior: one (IC 4296) shows a steep central increase of $\Sigma_X(R)$, due to an AGN that is producing a bright nuclear radio and X-ray source; the other (NGC 507), outside $10^{-2}R_{VIR}$, presents a brightness "excess," due to complex substructures in its halo, produced by a radio lobe, sloshing motions, and interactions with the nearby galaxy NGC499 (K19; M. Brienza et al. 2022).

5. Summary, Discussion, and Conclusions

In this work we have compared the X-ray properties of the gas-flow models of C22 with those observed for ETGs and collected in recent large and homogeneous studies based on Chandra data. The simulations of C22 were conducted with the high-resolution 2D hydrodynamical code MACER (G19b), for a set of realistic galaxies with three representative stellar masses; for each mass, three galaxy orbital structures were considered: the nonrotating case, the isotropic rotator, and an intermediate case with a radially declining ordered rotation. Mass sources are provided by stellar mass losses and by a

[11] The "double-break" type shows a $T_X(R)$ profile that is falling at small radii, rising at intermediate radii until the peak of the broad bump, and falling again at large radii. This and the HB types comprise 50% of the K20 sample (30 out of 60 galaxies).

cosmologically motivated time-dependent mass accretion rate imposed at the outer boundary of the numerical grid. Star formation, which takes place especially in the central gas disk, triggered by the Toomre instability, acts as a sink and source of mass, the latter due to SNe II explosions. Finally, SMBH accretion causes a self-consistently determined AGN feedback, both radiative and mechanical (due to AGN winds).

First, we compared with observations in the 0.3–8 keV band the global properties of the hot gas: the luminosity and the average temperature for the whole galaxy, L_X and $\langle T_X\rangle$, and those within $5R_e$, $L_{X,5}$ and $\langle T_{X,5}\rangle$. The models stay within, and cover most of, the observed distribution in the diagnostic planes L_X-L_K, $\langle T_{X,5}\rangle-L_K$, $L_X-\langle T_X\rangle$, and $L_{X,5}-\langle T_{X,5}\rangle$. The observed trend of more massive ETGs hosting on average more luminous and hotter halos is also reproduced. For each stellar mass, more rotating models are less X-ray-luminous, reinforcing previous results obtained for different galaxy structures, and also in the absence of AGN feedback and CGM accretion. At medium and high galaxy mass (for the MM and HM families), $\langle T_{X,5}\rangle$ is lower in rotating models, while the opposite is shown by the LM family. While $\langle T_{X,5}\rangle$ is sensitive to galactic properties, such as rotation, and to the presence of circumgalactic accretion, which increases its value, $\langle T_X\rangle$ instead depends mostly on the galaxy mass. Finally, CGM accretion can determine a large difference in L_X for models of same L_K. The general agreement of the C22 models with the observed global properties is not trivial, given that the input physics was chosen independently of the aim of reproducing the X-ray observations, and ranges from the galaxy dynamical structure and stellar evolution properties to a self-consistent description of the AGN feedback (within the limits of the central grid resolution of 25 pc) and to cosmological gas accretion.

In a second step, we compared the radial profiles of the surface brightness $\Sigma_X(R)$ and of the projected temperature $T_X(R)$ with those of the X-ray-bright elliptical NGC 5129, which is representative of the most common HB class of temperature profiles (K20). The L_K, R_e, σ_0, and flattening of NGC 5129 turned out to be similar to those of the HM models. These present three typical Σ_X shapes: the nonrotating HM_0 model has the most peaked profile, while ordered rotation creates a central flattening that becomes more pronounced for larger rotation. The Σ_X shape of the HM_0 and of the mildly rotating HM_k models follows quite well the observed one; a close match requires a model Σ_X upscale (of a factor of $\simeq$2.5) that could be produced by a uniform increase of the gas density by $\simeq$50%, as could be plausibly obtained for models tailored on NGC 5129. The T_X profile of the model instead looks problematic inside $R\approx 20$ kpc, where it is larger than in NGC 5129 and in some models shows unobserved spatial fluctuations; outside 20 kpc, instead, T_X is smooth and closer to the observed values and shape.

In order to better understand the origin of the T_X profile, additional simulations were performed for the more satisfactory HM_k model, keeping all its properties fixed. A model with a larger infall speed for the CGM (HM_k^{new}) turned out to compare better than HM_k with the observations of NGC 5129: at an age close to that of this galaxy, $T_X(R)$ within 20 kpc is smoother and lower, and outside 30 kpc it increases slightly—all features that bring the model closer to observations. However, $T_X(R)$ of HM_k^{new} remains larger than observed in the central region. A model without CGM accretion was also studied, finding that its L_X, $L_{X,5}$, $\langle T_X\rangle$, and $\langle T_{X,5}\rangle$ still fall within the observed range, but its $\Sigma_X(R)$ and $T_X(R)$ totally fail to reproduce those of NGC 5129: $\Sigma_X(R)$ becomes much more peaked, L_X is far below that of the galaxy, and $T_X(R)$ is decreased at all radii, especially outside $R\simeq 3$ kpc, and lacks the characteristic bump.

To extend the validity of the previous results, the more successful model HM_k^{new} was compared with other well-studied Chandra ETGs of the HB class. What was found in the detailed comparison with NGC 5129 was confirmed: the model represents an average of the observed $\Sigma_X(R)$ profiles normalized by their value at $0.01R_{VIR}$; it also falls within the observed temperature values, but it lies on their upper envelope within $\simeq 10^{-2}R_{VIR}$.

In conclusion, the C22 models are generally successful in reproducing the X-ray observations. However, in the central region, the model temperature appears systematically larger than observed, by $\simeq$30%–40%, as evidenced by the specific analysis based on NGC 5129 and extended to all the HB galaxies. No simple solution to this discrepancy has been found, but a few possibilities can be discussed. First, the presence of temporal and spatial fluctuations in the model $T_X(R)$ within a radius of a few kiloparsecs, which contrasts with the monotonic and constant-in-time $T_X(R)$ decline at large radii, indicates that the AGN feedback may have a too-strong effect within the central region. Therefore, one possibility is that the input physics of the AGN feedback should be revised in the values of some parameters. However, the mass, momentum, and energy injected by the AGN winds cannot be adjusted arbitrarily, because they obey physical balance relations that cannot be violated (J. P. Ostriker et al. 2010) and that are implemented in the MACER models. In addition, the AGN feedback efficiencies cannot be reduced much, to prevent an excessive growth of the SMBH.

A second possibility is suggested by the fact that the model $\Sigma_X(R)$ and $T_X(R)$ are overall close to those observed for NGC 5129. Under the assumption that the simulations are producing a pressure profile consistent with the real one, it is interesting to check the consequences of keeping this same pressure profile but with the temperature reduced by the required factor of $\alpha\simeq 1.4$–1.6 within $\simeq$20 kpc. This would increase the density by the same factor, and Σ_X by a factor of $\alpha^{3/2}\simeq 1.7$–2, for an emissivity proportional to $\rho^2\sqrt{T}$, and by $\alpha^2\simeq 2$–2.6, for a cooling function approximately constant with the temperature (as would be reasonable for a temperature within 40% of $kT\simeq 1$ keV). The resulting increase of Σ_X would be of a factor curiously close to that required in Section 4 to shift the model Σ_X upward and reach that of NGC 5129. We recall that in the simulations, the gas temperature is a derived quantity, obtained as the ratio between the gas pressure and density; thus, if for some reason the density in the simulations is lower than in NGC 5129, an overestimate of the temperature naturally follows. Of course, it should be checked whether the same argument can be applied to other ETGs in Figure 6 before this possibility can be proposed as a plausible solution.

A third effect that could lower the central $T_X(R)$ by 30%–40% would be present (but missing in the simulations) if the ISM is multiphase in a way requiring a 3D description. Indeed, colder gas phases have been observed in ETGs, especially if they are central dominant galaxies in groups and clusters (e.g., N. Werner et al. 2014; E. O'Sullivan et al. 2018), and multiphase gas has been found by 3D simulations (e.g.,

M. Gaspari et al. 2017; M. Guo et al. 2023). In Appendix B.1, we provide simple formulae for the expected change in L_X and T_X produced by inhomogeneities in pressure equilibrium with their surroundings. Changes in the sought direction and of the required size can be easily originated. For example, from Equation (B6), a two-phase inhomogeneous gas, with a density larger by a factor $r = 5$ in a volume fraction $v = 0.1$, has an emission-weighted temperature reduced to $\simeq$0.6 that of its homogeneous counterpart and a luminosity 1.7 times larger; for $r = 3$, increases in L_X of 30% and decreases in T_X of 25% are obtained for a broad range of $v \approx 0.1$–0.6 (these estimates adopt a cooling function roughly independent of the temperature). Therefore, 3D density inhomogeneities would reduce the T_X of the models, and they are especially expected in the central regions (e.g., M. Guo et al. 2023), where the model T_X appears too large.

Finally, some uncertainties could affect also the measured $T_X(R)$. For example, from Chandra data of NGC 5129, V. Bharadwaj et al. (2014) find an increasing profile from $kT_X = 0.9$ keV at a few kiloparsecs to $kT_X = 1.2$ keV between 30 and 40 kpc; J. M. Nugent et al. (2020) also found $kT_X = 0.85$ keV between a 2 and 3 kpc radius, and a peak value of 1.25 keV between 10 and 20 kpc. These temperatures are larger than those in Figures 4 and 5, and closer to the model ones; however, the authors above also measured larger temperatures outside the peak position: for example, at 60 kpc radius, $kT_X = 1$ keV (V. Bharadwaj et al. 2014) and 1.1 keV (J. M. Nugent et al. 2020), while $kT_X \simeq 0.85$ keV in the model. In addition, as shown in Section 4.1, within $\simeq 10^{-2} R_{VIR}$, the model $T_X(R)$ seems larger than for most ETGs of the HB class, and thus possible measurement uncertainties for NGC 5129 cannot be a general solution.

The analysis in this work has shown the potential of a close comparison between the results of high-resolution hydrodynamical simulations and data products from X-ray observatories such as Chandra. In particular, the C22 MACER exploratory set of models highlighted the importance of CGM accretion in accomplishing an agreement with the observed results, thanks to its effect of enhancing L_X (and also $\langle T_X \rangle$, to a lower extent) and of producing a radially extended X-ray surface brightness profile and large temperature values in the outer galactic region. The comparison also highlighted a small but systematic discrepancy in the temperatures inside (1–2)R_e, which calls for simulations even more closely tailored to observed galaxies, and/or for a wider exploration of the parameters describing AGN accretion and feedback, and/or for 3D simulations capable of fully accounting for multiphase effects.

Acknowledgments

The referee is thanked for useful suggestions. L.C. and S.P. acknowledge support from the project PRIN MUR 2022 (code 2022ARWP9C), "Early Formation and Evolution of Bulge and HalO (EFEBHO)," PI: M. Marconi, funded by European Union—Next Generation EU (CUP J53D23001590006). The simulations analyzed in this work were performed with the Princeton Research Computing resources at Princeton University, which is a consortium of groups, including the Princeton Institute for Computational Science and Engineering and the Princeton University Office of Information Technology's Research Computing department.

Appendix A
Radiative Transfer and Computation of Observable Quantities in the X-Rays

We describe here the procedure adopted to compute the emergent emission and then the surface brightness Σ_X and the projected temperature T_X of the model galaxies. In the C22 MACER simulations, cold gas, or even a high-surface-density circumnuclear disk, can be present in the central regions, and these can be opaque to X-rays. In addition, wherever star formation takes place, it is associated with a metal enrichment that contributes to modifying the X-ray emission and absorption. X-ray absorption can be significant, especially when looking through the disk from an edge-on view, as supposed in this work.

A.1. Transmission of the Spectrum

We calculate first the radiative transfer along the line of sight, by postprocessing the hydrodynamical simulation data. The radiative transfer equation (e.g., S. Chandrasekhar 1960) reads as

$$\frac{dI_\nu}{ds} = -\alpha_\nu I_\nu + j_\nu, \tag{A1}$$

where I_ν is the radiation field specific intensity we aim to evaluate, and s is the distance measured along an arbitrary line of sight starting from some origin. j_ν and α_ν are, respectively, the emission and absorption coefficients per unit volume and are derived from the atomic processes as described below (Appendix A.2); for simplicity, we ignore scattering processes. The integration of Equation (A1) leads to the formal solution

$$I_\nu(\tau_\nu) = I_\nu(0)\, e^{-\tau_\nu} + \int_0^{\tau_\nu} S_\nu(\tau'_\nu)\, e^{-(\tau_\nu - \tau'_\nu)}\, d\tau'_\nu, \tag{A2}$$

where

$$S_\nu \equiv \frac{j_\nu}{\alpha_\nu}, \quad \tau_\nu \equiv \int_0^s \alpha_\nu(s')\, ds' \tag{A3}$$

are, respectively, the source function and the optical depth along the line of sight measured from the origin. Ignoring the background radiation $I_\nu(0)$, and recasting the integration in terms of s, Equation (A2) gives the specific intensity emerging at s due to emission and absorption processes of the material between 0 and s:

$$I_\nu(0, s) = \int_0^s j_\nu(s')\, e^{-\tau_\nu(s', s)}\, ds',$$
$$\tau_\nu(s', s) \equiv \int_{s'}^{s} \alpha_\nu(s'')\, ds'', \tag{A4}$$

where the meaning of $\tau_\nu(s', s)$ is obvious.

A.2. Atomic Processes

Here, we show how the emission and absorption coefficients j_ν and α_ν were derived, starting from the gas temperature T, the hydrogen and electron number densities n_H and n_e, and the chemical composition that were derived for the gas during the simulations. We recall that the adopted metal abundances are $Z_* = 1.5 Z_\odot$, where $Z_\odot = 0.0134$ (M. Asplund et al. 2009), for the stellar population of the massive ETGs, and $Z_{CGM} = 0.15 Z_\odot$, for the accreting CGM (C22). During

evolution, the ISM is enriched by the nucleosynthetic yields of SNe Ia and SNe II, the latter being injected by new star formation, transported around mostly by AGN winds, and diluted by CGM accretion (Z. Gan et al. 2019a; S. Pellegrini et al. 2020).

We first evaluated the frequency-dependent emissivity ϵ_ν, i.e., the radiated power per unit volume per unit frequency:

$$\epsilon_\nu = n_{\rm H} n_e \Lambda_\nu, \tag{A5}$$

where Λ_ν is the cooling function per unit frequency and depends on the temperature T and on the chemical composition. Λ_ν was evaluated by using the software package ATOMDB (version 3.0.9; assuming collisional ionization equilibrium). Assuming that the X-ray emission is isotropic, the emission coefficient j_ν is simply given by

$$j_\nu = \frac{\epsilon_\nu}{4\pi}. \tag{A6}$$

The absorption coefficient α_ν is a function of the gas density and metal abundance. For the solar abundance, we adopt the photoelectric absorption cross section $\sigma_{\nu,\rm solar} = \sigma_{\nu,\rm H+He} + \sigma_{\nu,\rm metal}$ of D. Morrison & G. McCammon (1983), in which H and He contribute $\sigma_{\nu,\rm H+He}$ and dominate the cross section for soft-X-ray photons ($E \lesssim 0.5$ keV), while the absorption of hard-X-ray photons is mainly contributed by metals (elements heavier than He). Assuming that the X-ray absorption by the metal-rich ISM can be written as a linear function of the metallicity Z (in units of solar metallicity $Z_\odot$), we adopt

$$\sigma_\nu = \sigma_{\nu,\rm H+He} + Z \times \sigma_{\nu,\rm metal}. \tag{A7}$$

The absorption coefficient is then given by

$$\alpha_\nu = n_{\rm H} \sigma_\nu. \tag{A8}$$

A.3. X-Ray Surface Brightness, Luminosity, Temperature Profile, and Average Temperatures for the Models

Using Equations (A4), (A6), and (A8), we can derive the observed properties of the models in the X-ray band, which in this work we take as the broad Chandra band of 0.3–8 keV. To evaluate the radiative transfer, we perform the calculations in a fashion of ray tracing—i.e., we integrate Equation (A4) along the direction from the emitter to the observer. The radiation in and behind the circumnuclear gaseous disk is attenuated whenever the disk is optically thick; this especially affects the soft X-rays. In the MACER simulations, spherical coordinates —with a logarithmic radial grid to cover a large dynamical range, from $r = 2.5$ pc to $\sim$250 kpc in the highest-resolution runs—make the integration along the straight line s not immediate. We then interpolate the gridded data from the original spherical coordinates onto a new cylindrical coordinate system $(z, \tilde{r}, \varphi)$, with the z-axis along the line of sight pointing toward the observer, so that the numerical integration reduces to a summation along the z-axis of the new cylindrical coordinate system. Moreover, to preserve the high resolution in the galactic central regions, we adopt logarithmic spacing in both the z- and $\tilde{r}$-directions. We thus integrate Equation (A4) for fixed $(\tilde{r}, \varphi)$ in the projection plane, with s replaced by z and spanning the whole interval $(z_{\rm min}, z_{\rm max})$ covered by the numerical grid, to obtain the monochromatic 2D brightness distribution Σ_ν and then the X-ray surface brightness $\Sigma_{\rm X}$ after integration over the energy band of interest:

$$\Sigma_\nu(\tilde{r}, \varphi) = 4\pi I_\nu(z_{\rm min}, z_{\rm max}),$$
$$\Sigma_{\rm X}(\tilde{r}, \varphi) = \int_{\nu_{\rm min}}^{\nu_{\rm max}} \Sigma_\nu(\tilde{r}, \varphi)\, d\nu. \tag{A9}$$

The total X-ray luminosity $L_{\rm X}$ is evaluated by integrating $\Sigma_{\rm X}$ over the surface area $dA = \tilde{r}\, d\tilde{r} d\varphi$ on the sky plane—i.e.,

$$L_{\rm X} = \int \Sigma_{\rm X}(\tilde{r}, \varphi)\, dA. \tag{A10}$$

If the integration is performed within a radius of $5R_{\rm e}$, one obtains $L_{\rm X,5}$, the luminosity within a cylinder, with its axis along the line of sight and with a base circle of radius $5R_{\rm e}$.

In the analysis of X-ray observations, the temperature $T_{\rm X}$ is derived from the X-ray spectra, and it is an emission-weighted quantity, with good approximation (e.g., K19; N. Truong et al. 2020). Therefore, as a proxy for $T_{\rm X}$, we evaluate the projection of the gas temperature T along the line of sight, weighting it by the X-ray emission after absorption:

$$T_{\rm X}(\tilde{r}, \varphi) = \frac{\int_{\nu_{\rm min}}^{\nu_{\rm max}} d\nu \int_{z_{\rm min}}^{z_{\rm max}} T(z)\, j_\nu(z)\, e^{-\tau_\nu(z, z_{\rm max})}\, dz}{\int_{\nu_{\rm min}}^{\nu_{\rm max}} d\nu \int_{z_{\rm min}}^{z_{\rm max}} j_\nu(z)\, e^{-\tau_\nu(z, z_{\rm max})}\, dz}. \tag{A11}$$

Finally, we calculate the circularized surface brightness profile $\Sigma_{\rm X}(R)$ and the circularized surface-brightness-weighted temperature profile $T_{\rm X}(R)$ as angle-averaged quantities over the annulus $R - \Delta R/2 < \tilde{r} < R + \Delta R/2$:

$$\Sigma_{\rm X}(R) = \frac{\int_0^{2\pi} \int_{R-\Delta R/2}^{R+\Delta R/2} \Sigma_{\rm X}(\tilde{r}, \varphi)\, dA}{2\pi R \Delta R},$$
$$T_{\rm X}(R) = \frac{\int_0^{2\pi} \int_{R-\Delta R/2}^{R+\Delta R/2} T_{\rm X}(\tilde{r}, \varphi)\, \Sigma_{\rm X}(\tilde{r}, \varphi)\, dA}{\int_0^{2\pi} \int_{R-\Delta R/2}^{R+\Delta R/2} \Sigma_{\rm X}(\tilde{r}, \varphi)\, dA}. \tag{A12}$$

For the comparison with the average temperature observed within a given aperture (e.g., $5R_{\rm e}$), we define for the models

$$\langle T_{\rm X} \rangle (R) = \frac{\int_0^R \Sigma_{\rm X}(R')\, T_{\rm X}(R')\, R'\, dR'}{\int_0^R \Sigma_{\rm X}(R')\, R'\, dR'}. \tag{A13}$$

The average temperature over the whole galaxy is indicated with $\langle T_{\rm X} \rangle$ and that within $5R_{\rm e}$ (i.e., $\langle T_{\rm X} \rangle (5R_{\rm e})$) with $\langle T_{\rm X,5} \rangle$.

Appendix B
Effects of a Multiphase Medium on Observed Temperature and Luminosity

As discussed in Section 5, the emission-weighted temperature can be reduced in a multiphase medium, with a reduction factor comparable to that needed to bring the model profiles in better agreement with the observed ones. The C22 simulations are 2D, and it is reasonable to expected that in a high-resolution 3D simulation, the number of inhomogeneities for the unit volume would increase, especially in the inner galactic regions, where AGN feedback heats and compresses the gas (discussed in Appendix B.1). Another possible source of ISM inhomogeneities involves the process of 3D fragmentation of the cold gaseous disk (discussed in Appendix B.2).

B.1. Emission-weighted Average Temperature and Luminosity of a Multiphase Medium

We present here a simple model to estimate the effects of a multiphase medium on the luminosity and on the luminosity-weighted temperature measured when averaging over a sufficiently large volume. We consider first a volume V, filled with a gas of uniform density ρ, with total mass $M = \rho V$ and uniform temperature T; the pressure is $p = k_B \rho T/(\mu m_p)$, and the total internal energy is $U = (3/2)pV$. The emission per unit volume is assumed to be $A\rho^2 T^\lambda$, with A and λ given constants; in this way, the total luminosity of the gas is $L = A\rho^2 T^\lambda V$. We now consider what luminosity $L_{\rm multi}$ and emission-weighted temperature $T_{\rm multi}$ are obtained if the same volume V contains the same amount of gas M but the gas is distributed in N different phases of density ρi, each occupying the volume V_i; moreover, we assume pressure equilibrium between the different phases—i.e., $p_1 = p_2 = ... = p_N$—and we also require that the total internal energy of the nonhomogeneous configuration is the same as for the homogeneous system. We define the normalized quantities

$$\tilde{V}_i \equiv \frac{V_i}{V}, \quad \tilde{\rho}_i \equiv \frac{\rho_i}{\rho}, \tag{B1}$$

and we have

$$\sum_{i=1}^{N} \tilde{V}_i = 1, \quad \sum_{i=1}^{N} \tilde{\rho}_i \tilde{V}_i = 1, \quad T_i = \frac{T}{\tilde{\rho}_i}. \tag{B2}$$

Therefore, for the multiphase gas, the luminosity $L_{\rm multi}$ and the temperature $T_{\rm multi}$ are:

$$\begin{aligned} L_{\rm multi} &\equiv \sum_{i=1}^{N} L_i = L \times \sum_{i=1}^{N} \tilde{\rho}_i^{2-\lambda} \tilde{V}_i, \\ T_{\rm multi} &\equiv \frac{\sum_{i=1}^{N} L_i T_i}{L_{\rm multi}} = T \times \frac{\sum_{i=1}^{N} \tilde{\rho}_i^{1-\lambda} \tilde{V}_i}{\sum_{i=1}^{N} \tilde{\rho}_i^{2-\lambda} \tilde{V}_i}, \end{aligned} \tag{B3}$$

as expected, for $\lambda = 1$, $L_{\rm multi} = L$, and $T_{\rm multi} = T$. In order to obtain a numerical estimate, we consider the simple case of a two-phase medium, where we introduce the density ratio between the high- and low-density phases and the corresponding volume ratio:

$$r \equiv \frac{\rho_{\rm high}}{\rho_{\rm low}}, \quad v \equiv \frac{V_{\rm high}}{V_{\rm low}}. \tag{B4}$$

From the general relations, it follows that

$$\begin{aligned} \tilde{\rho}_{\rm high} &= r\tilde{\rho}_{\rm low}, \quad \tilde{V}_{\rm high} = v\tilde{V}_{\rm low}, \\ \tilde{\rho}_{\rm low} &= \frac{1+v}{1+rv}, \quad \tilde{V}_{\rm low} = \frac{1}{1+v}, \end{aligned} \tag{B5}$$

so that

$$\begin{aligned} L_{\rm multi} &= L \times \frac{(1+v)^{1-\lambda}(1+r^{2-\lambda}v)}{(1+rv)^{2-\lambda}}, \\ T_{\rm multi} &= T \times \frac{(1+rv)(1+r^{1-\lambda}v)}{(1+v)(1+r^{2-\lambda}v)}. \end{aligned} \tag{B6}$$

These formulae are used in Section 5 to assess the effect of density inhomogeneities on the luminosity and temperature measured for a region hosting them. For $\lambda < 1$, at any v, the luminosity is enhanced ($L_{\rm multi} > L$), and the temperature is reduced ($T_{\rm multi} < T$), and these variations are larger for larger r. Note that a density ratio of r corresponds to a temperature ratio of $1/r$; thus, if r is small (say $\lesssim$5), and the temperature of the homogeneous configuration is such that the gas emits in the X-ray band, the temperatures of the different phases remain within a range where most of the emission is in the X-ray band, and Equation (B6) can be used to obtain the multiphase L_X and T_X.

B.2. Fragmentation in a Central Gaseous Disk

We give here a simple argument by which 3D instabilities are to be expected in the cold rotating disk subject to Toomre instability. As implemented in the code, at radius R, the disk becomes locally unstable when

$$Q_T(R) = \frac{c_D(R)\kappa_R(R)}{\pi G \Sigma(R)} < 1, \tag{B7}$$

where $\Sigma(R)$, $c_D(R)$, and $\kappa_R(R)$ are respectively the local gas surface density, speed of sound, and radial epicyclic frequency. Assuming for simplicity a roughly constant disk rotational velocity $V_{\rm rot}$, then $\kappa_R = \sqrt{2}\, V_{\rm rot}/R$, and so for a marginally stable disk at R,

$$\Sigma_T(R) \equiv \frac{c_D(R)\kappa_R(R)}{\pi G} = \frac{\sqrt{2}}{\pi}\frac{c_D(R)V_{\rm rot}}{GR}. \tag{B8}$$

We now assume that a region of radius r_J around R collapses due to the Jeans instability, so that from the identities

$$M_J \equiv \frac{4\pi}{3} r_J^3 \rho_J = \pi r_J^2 \Sigma_T(R), \quad r_J = \sqrt{\frac{\pi}{4G\rho_J}}\, c_D(R), \tag{B9}$$

we can express the various quantities in terms of the properties of the disk as

$$\begin{aligned} r_J &= \frac{\pi c_D(R)^2}{3G\Sigma_T(R)} = \frac{\pi^2 c_D(R) R}{3\sqrt{2}\, V_{\rm rot}}, \quad \rho_J = \frac{9G\Sigma_T(R)^2}{4\pi c_D(R)^2} = \frac{9V_{\rm rot}^2}{2\pi^3 G R^2}, \\ M_J &= \frac{\pi^3 c_D(R)^4}{9G^2\Sigma_T(R)} = \frac{\pi^4 c_D(R)^3 R}{9\sqrt{2}\, G V_{\rm rot}}. \end{aligned} \tag{B10}$$

Therefore, as an order-of-magnitude estimate, the first of the equations above indicates that a Toomre-unstable ring, in a disk with $V_{\rm rot} = 100$ km s^{-1} and $T_{\rm disk} = 100$ K, would fragment in a number $\pi R/r_J \approx 100$ blobs, which would cool, collapse, and increase their density.

ORCID iDs

Silvia Pellegrini https://orcid.org/0000-0002-8974-2996
Luca Ciotti https://orcid.org/0000-0002-5708-5274
Zhaoming Gan https://orcid.org/0000-0003-3886-0383
Dong-Woo Kim https://orcid.org/0000-0002-7386-944X
Jeremiah P. Ostriker https://orcid.org/0000-0002-6405-9904

References

Asplund, M., Grevesse, N., Sauval, A. J., et al. 2009, ARA&A, 47, 481
Babyk, I. V., McNamara, B. R., Nulsen, P. E. J., et al. 2018, ApJ, 857, 32
Bharadwaj, V., Reiprich, T. H., Schellenberger, G., et al. 2014, A&A, 572, 46
Boroson, B., Kim, D.-W., & Fabbiano, G. 2011, ApJ, 729, 12
Brienza, M., Lovisari, L., Rajpurohit, K., et al. 2022, A&A, 661, 92

Brighenti, F., Mathews, W. G., Humphrey, P. J., & Buote, D. A. 2009, ApJ, 705, 1672
Chandrasekhar, S. 1960, Radiative Transfer (New York: Dover)
Choi, E., Ostriker, J. P., Naab, T., Oser, L., & Moster, B. P. 2015, MNRAS, 449, 4105
Ciotti, L., Mancino, A., Pellegrini, S., & Ziaee Lorzad, A. 2021, MNRAS, 500, 1054
Ciotti, L., & Ostriker, J. P. 2001, ApJ, 551, 131
Ciotti, L., & Ostriker, J. P. 2007, ApJ, 665, 1038
Ciotti, L., & Ostriker, J. P. 2012, in Hot Interstellar Matter in Elliptical Galaxies, ed. D.-W. Kim & S. Pellegrini (New York: Springer), 83
Ciotti, L., Ostriker, J. P., Gan, Z., et al. 2022, ApJ, 933, 154
Ciotti, L., Pellegrini, S., Negri, A., & Ostriker, J. P. 2017, ApJ, 835, 15
Eckmiller, H. J., Hudson, D. S., & Reiprich, T. H. 2011, A&A, 535, 105
Eskridge, P. B., Fabbiano, G., & Kim, D.-W. 1995, ApJS, 97, 141
Gan, Z., Choi, E., Ostriker, J. P., Ciotti, L., & Pellegrini, S. 2019a, ApJ, 875, 109
Gan, Z., Ciotti, L., Ostriker, J. P., & Yuan, F. 2019b, ApJ, 872, 167
Gan, Z., Hensley, B. S., Ostriker, J. P., et al. 2020, ApJ, 901, 7
Gaspari, M., Temi, P., & Brighenti, F. 2017, MNRAS, 466, 677
Goulding, A.D., Greene, J. E., Ma, C.-P., et al. 2016, ApJ, 826, 167
Gu, M., Greene, J., Newman, A. B., et al. 2022, ApJ, 932, 103
Guo, M., Stone, J. M., Kim, C.-G., & Quataert, E. 2023, ApJ, 946, 26
Helsdon, S. F., & Ponman, T. J. 2003, MNRAS, 340, 485
Islam, N., Kim, D.-W., Lin, K., et al. 2021, ApJS, 256, 22
Jaffe, W. 1983, MNRAS, 202, 995
Juranova, A., Werner, N., Nulsen, P. E. J., et al. 2020, MNRAS, 499, 5163
Kim, D.-W., Anderson, C., Burke, D., et al. 2019, ApJS, 241, 36
Kim, D.-W., & Fabbiano, G. 2015, ApJ, 812, 127
Kim, D.-W., Traynor, L., Paggi, A., et al. 2020, MNRAS, 492, 2095
Lakhchaura, K., Werner, N., Sun, M., et al. 2018, MNRAS, 481, 4472
Li, M., Li, Y., Bryan, G. L., Ostriker, E. C., & Quataert, E. 2020, ApJ, 898, 23
Mohapatra, R., Quataert, E., Fielding, D., & Guo, M. 2025, ApJ, 989, 103
Morrison, D., & McCammon, G. 1983, ApJ, 400, 699
Nardini, E., Kim, D.-W., & Pellegrini, S. 2022, in Handbook of X-ray and Gamma-ray Astrophysics, ed. C. Bambi & A. Santangelo (Singapore: Springer), 4321
Negri, A., Ciotti, L., & Pellegrini, S. 2014a, MNRAS, 439, 823
Negri, A., Posacki, S., Pellegrini, S., & Ciotti, L. 2014b, MNRAS, 445, 1351
Nugent, J. M., Dai, X., & Sun, M. 2020, ApJ, 899, 160
Ostriker, J. P., Choi, E., Ciotti, L., et al. 2010, ApJ, 722, 642
O'Sullivan, E., Combes, F., Salomé, P., et al. 2018, A&A, 618, 126
Pellegrini, S. 2012, in Hot Interstellar Matter in Elliptical Galaxies, ed. D.-W. Kim & S. Pellegrini (New York: Springer), 21
Pellegrini, S., Ciotti, L., Negri, A., & Ostriker, J. P. 2018, ApJ, 856, 115
Pellegrini, S., Gan, Z., Ostriker, J. P., & Ciotti, L. 2020, AN, 341, 184
Posacki, S., Pellegrini, S., & Ciotti, L. 2013, MNRAS, 433, 2259
Sarzi, M., Alatalo, K., Blitz, L., et al. 2013, MNRAS, 432, 1845
Satoh, C. 1980, PASJ, 32, 41
Stone, J. M., Tomida, K., White, C. J., & Felker, K. G. 2020, ApJS, 249, 4
Truong, N., Pillepich, A., Werner, N., et al. 2020, MNRAS, 494, 549
Veale, M., Ma, C.-P., Thomas, J., et al. 2017, MNRAS, 464, 356
Wang, C., Li, Y., & Ruszkowski, M. 2019, MNRAS, 482, 3576
Werner, N., Oonk, J. B. R., Sun, M., et al. 2014, MNRAS, 439, 2291